



Article

Ni-Based Hydrotalcite (HT)-Derived Cu Catalysts for Catalytic Conversion of Bioethanol to Butanol

Yan Xiao ^{1,†}, Jie Li ^{1,†}, Yuan Tan ^{1,*} , Xingkun Chen ¹, Fenghua Bai ², Wenhao Luo ² and Yunjie Ding ^{3,4,*}

¹ Hangzhou Institute of Advanced Studies, Zhejiang Normal University, 1108 Gengwen Road, Hangzhou 311231, China; xiaoyan@dicp.ac.cn (Y.X.); lijie_zjnu@163.com (J.L.)

² School of Chemistry and Chemical Engineering, Inner Mongolia University, 235 West University Street, Hohhot 010021, China; w.luo@imu.edu.cn (W.L.)

³ Dalian National Laboratory for Clean Energy, Dalian Institute of Chemical Physics, Chinese Academy of Sciences, Dalian 116023, China

⁴ The State Key Laboratory of Catalysis, Dalian Institute of Chemical Physics, Chinese Academy of Sciences, Dalian 116023, China

* Correspondence: yuantan2012@zjnu.edu.cn (Y.T.); dyj@dicp.ac.cn (Y.D.); Tel.: +86-571-8225-7902 (Y.T.); +86-411-8437-9143 (Y.D.)

† These authors contributed equally to this work.

Abstract: Catalytic conversion of biomass-derived ethanol into n-butanol through Guerbet coupling reaction has become one of the key reactions in biomass valorization, thus attracting significant attention recently. Herein, a series of supported Cu catalysts derived from Ni-based hydrotalcite (HT) were prepared and performed in the continuous catalytic conversion of ethanol into butanol. Among the prepared catalysts, Cu/NiAlO_x shows the best performance in terms of butanol selectivity and catalyst stability, with a sustained ethanol conversion of ~35% and butanol selectivity of 25% in a time-on-stream (TOS) of 110 h at 280 °C. While for the Cu/NiFeO_x and Cu/NiCoO_x, obvious catalyst deactivation and/or low butanol selectivity were obtained. Extensive characterization studies of the fresh and spent catalysts, i.e., X-ray diffraction (XRD), Transmission electron microscopy (TEM), X-ray photoelectron spectroscopy (XPS) and Hydrogen temperature-programmed reduction (H₂-TPR), reveal that the catalysts' deactivation is mainly caused by the support deconstruction during catalysis, which is highly dependent on the reducibility. Additionally, an appropriate acid–base property is pivotal for enhancing the product selectivity, which is beneficial for the key process of aldol-condensation to produce butanol.

Keywords: Ni-based hydrotalcite; biomass conversion; support effect; selectivity; stability



Citation: Xiao, Y.; Li, J.; Tan, Y.; Chen, X.; Bai, F.; Luo, W.; Ding, Y. Ni-Based Hydrotalcite (HT)-Derived Cu Catalysts for Catalytic Conversion of Bioethanol to Butanol. *Int. J. Mol. Sci.* **2023**, *24*, 14859. <https://doi.org/10.3390/ijms241914859>

Academic Editor: Haiyang Gao

Received: 30 August 2023

Revised: 27 September 2023

Accepted: 1 October 2023

Published: 3 October 2023



Copyright: © 2023 by the authors. Licensee MDPI, Basel, Switzerland. This article is an open access article distributed under the terms and conditions of the Creative Commons Attribution (CC BY) license (<https://creativecommons.org/licenses/by/4.0/>).

1. Introduction

Production of value-added fuels, chemicals and materials from abundant, renewable resources such as biomass and its derivatives could provide a feasible route to alleviate our dependence on dwindling fossil fuels [1,2]. Bioethanol is a promising platform molecule derived from biomass, which could be produced from the fermentation of sugar-containing crops [3,4]. Over the last decades, the catalytic upgrading of bioethanol into high-value-added chemicals, such as aldehyde, butanol, ethyl acetate and butadiene, has attracted great interest worldwide [5–7].

Butanol is an important commodity chemical which can be used for the production of a plethora of value-added end products with various applications [8,9]. It has been recognized as a promising alternative to gasoline owing to its excellent fuel properties and good compatibility [10,11]. Traditionally, butanol has been produced through oxo process (hydroformylation of propylene) or the fermentation of sugars—the acetone, butanol and ethanol (ABE) process [12,13]. However, the former depends heavily on the use of a fossil resource as raw material, and the latter process suffers from its long-time fermentation procedure and low production efficiency of butanol [12,13]. Alternatively, the

catalytic upgrading of bioethanol into butanol through the Guerbet coupling process has attracted widespread attention both in academia and industry [14–16]. This is a well-known industrial route for higher alcohol synthesis and involves a tandem reaction route with several steps, including ethanol dehydrogenation to acetaldehyde, aldol condensation of acetaldehyde to 3-hydroxybutyraldehyde, dehydration of 3-hydroxybutyraldehyde to crotonaldehyde, and the hydrogenation of crotonaldehyde to butanol [17–19].

Many examples of heterogeneous catalysts are now available for the Guerbet coupling reaction, including hydroxyapatites [12,20], metal oxides [21,22], basic zeolites [23,24], and hydrotalcite (HT)-derived mixed oxides [25–30]. However, their catalytic performances are usually unsatisfactory due to the harsh reaction conditions [12,31,32]. The presence of transition metal active sites has been found to promote hydrogen transfer and greatly increase ethanol transformation [26,28,29]. Among these, Cu-based and Ni-based catalysts are promising candidates due to their low price and excellent hydrogenation capability [22,29,33]. Pang et al. have reported the effectiveness of Ni-MgAlO catalysts for continuous catalytic ethanol conversion to butanol [16]. The optimal Ni₄MgAlO (19.5 wt.% Ni) catalyst shows 18.7% of ethanol conversion and 55.2% of n-butanol selectivity. G. W. Huber et al. investigated Cu/Mg_xAlO_y catalysts for higher alcohol synthesis from ethanol, and found that the catalysts with low Cu loadings (0.1–0.6 wt.% Cu) show high selectivity to linear chain alcohols, while the catalyst with higher Cu loadings (>1.2 wt.% Cu) show high selectivity to ethyl acetate and acetone [27]. Recently, our group found that the addition of a small amount of Cu (>0.75 wt.%) to NiAlO_x can significantly improve the catalytic performance and afford a sustained ethanol conversion of ~35% and butanol selectivity of ~45% within 1000 h at 250 °C, 3 MPa N₂ [33]. However, when the support of NiAlO_x was replaced by ZnAlO_x, the product distribution changed greatly, with a large amount of ethyl acetate (Sel. of 42%) appearing in the system [34]. Previously, Boscolo et al. also found that the ethanol conversion, product selectivity and carbon deposition would be greatly affected by the support component, as the Mg²⁺ ion was partially substituted by Fe²⁺, Co²⁺, Ni²⁺, Cu²⁺ and Zn²⁺ ions [21]. These results strongly suggest that the role of support makes a large difference to catalytic performance. However, the origin of the support effect is still lacking evidence.

Herein, a series of Ni-based mixed-oxide-supported Cu catalysts were prepared and investigated for continuous catalytic conversion of ethanol into butanol. The activity, selectivity, and stability of different Cu/NiMO_x catalysts (i.e., Cu/NiAlO_x, Cu/NiFeO_x and Cu/NiCoO_x) were assessed and compared at 280 °C, 2 MPa N₂. Notably, compared with Cu/NiFeO_x and Cu/NiCoO_x, Cu/NiAlO_x outperforms markedly in butanol selectivity and stability. Based on systematic and complementary characterization studies of those fresh and spent catalysts, insights into the support effect on selectivity and stability were provided, together with the related reasons for the sustained superior performance of Cu/NiAlO_x.

2. Results

2.1. N₂ Physisorption Analysis of the Cu/NiMO_x Catalysts

The Ni-based HT-derived Cu catalysts (Cu/NiMO_x), with a similar Cu loading of ~1.5 wt%, were synthesized via the hydrothermal deposition precipitation method. The textural properties of three catalysts (i.e., Cu/NiAlO_x, Cu/NiFeO_x and Cu/NiCoO_x) were characterized by N₂ physical adsorption–desorption measurements. The results of specific surface area (S_{BET}), pore volume and pore size are listed in Table 1. The S_{BET} of three catalysts falls in the range of 209 to 260 m²/g, as the Ni-based mixed oxides varied among Al, Fe and Co. Similar values of the pore volumes and pore sizes are also observed for all three of the catalysts, indicating a similar structure for all of the mixed oxides. Furthermore, the obvious type IV isotherms with H4 hysteresis loops observed for the three catalysts indicate the presence of mesopores in all catalysts (Figure 1a) [35]. This is in line with the appearance of mesopores with a pore width of 3 to 8 nm determined by the Barrett–Joyner–Halenda (BJH) method, shown in the pore size distribution curves

(Figure 1b). The actual metal loadings of copper were determined by inductively coupled plasma atomic emission spectroscopy (ICP-AES), from which all catalysts show a similar value of ~1.5 wt.% (Table 1).

Table 1. Textural properties of different supported copper catalysts.

Entry	Catalysts	Cu Loadings (%) ^a	Specific Surface Area (m ² /g) ^b	Total Volume (cm ³ /g) ^b	Pore Size (nm) ^b
1	Cu/NiAlO _x	1.6	260	0.29	1.93
2	Cu/NiFeO _x	1.5	223	0.23	1.92
3	Cu/NiCoO _x	1.3	209	0.24	1.93

^a As determined by ICP-AES; ^b As determined by N₂ physisorption.

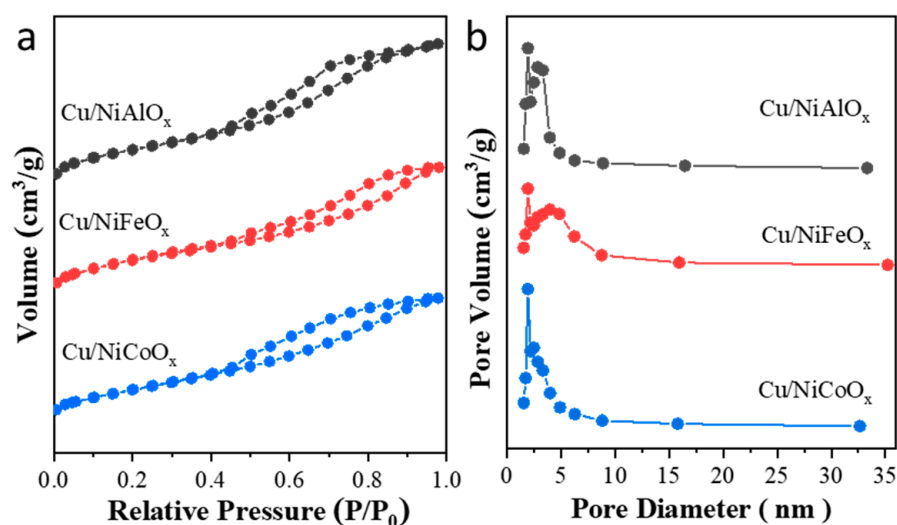


Figure 1. (a) N₂ physical adsorption–desorption isotherms and (b) BJH pore size distributions of different supported copper catalysts.

2.2. XRD Analysis of the Cu/NiMO_x Catalysts

The X-ray diffraction (XRD) patterns of Ni-based HT-derived Cu catalysts before and after the reaction are displayed in Figure 2. All catalysts display similar phase structures before the reaction, with diffraction peaks at 37.1°, 43.1° and 62.6°, respectively, which are the characteristic reflections of the (111), (200) and (220) crystal phases of NiO (Figure 2a). Furthermore, before the reaction, no diffraction peaks of metallic Cu can be observed, implying that the homogeneous distribution of Cu species or the Cu content is below the detection limit. For the spent Cu/NiAlO_x, Cu/NiFeO_x and Cu/NiCoO_x catalysts, it can be found that the metallic Ni clearly appeared. The diffraction peaks at 39.7°, 41.8° and 45.1° can be assigned to the characteristic reflections of (100), (002) and (101) planes of hexagonal Ni. The diffraction peaks at 44.5°, 51.8° and 76.3° can be due to the reflections of (111), (200) and (220) planes of cubic Ni (Figure 2b). For the spent Cu/NiAlO_x and Cu/NiFeO_x catalysts, both display mixed phases of hexagonal Ni and oxides. However, for the spent Cu/NiCoO_x, only bulk Ni can be detected, evidenced by the symmetrical and sharp diffraction peaks of cubic Ni. As significantly reduced Ni phases appeared in all catalysts, the reduction atmosphere during the Guerbet coupling process can be confirmed. This is consistent with previous studies in which the H-transfer process appeared in the Guerbet coupling process, thereby producing in-situ formed hydrogen (from ethanol dehydrogenation) and playing a role as reducing agent [36]. Thus, the nickel species can be reduced during catalysis. However, the metallic Cu cannot be observed, which might be attributed to the low content. Furthermore, according to the Scherrer equation, the larger Ni particle sizes of the spent Cu/NiFeO_x and Cu/NiCoO_x (~30 nm) catalysts can

be determined compared with those of the spent Cu/NiAlO_x (~20 nm), implying a severe agglomeration of Ni species for the Cu/NiFeO_x and Cu/NiCoO_x during catalysis.

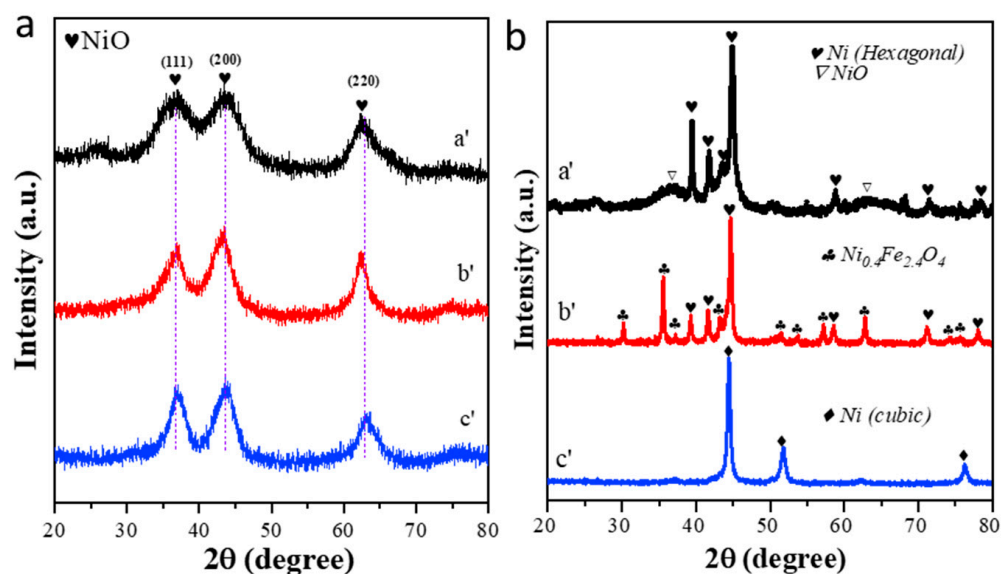


Figure 2. XRD patterns of different Ni-based HT-derived Cu catalysts before (a) and after (b) the reaction: (a') Cu/NiAlO_x; (b') Cu/NiFeO_x; (c') Cu/NiCoO_x.

2.3. TEM Analysis of the Cu/NiMO_x Catalysts

Transmission electron microscopy (TEM) and high-resolution TEM (HRTEM) were employed to study the microstructures of the Cu/NiMO_x catalysts before and after the reaction. In the fresh catalysts, no big metal particles could be observed in TEM images, as displayed in Figure 3a–c. By calculating the lattice parameter of the HRTEM images (Figure 3a'–c'), NiO(200) and NiO(111), with interplanar crystal spacings of ~2.1 Å and ~2.5 Å, respectively, could be discerned in all catalysts. This indicates that Ni existed as NiO and was homogeneously dispersed on the catalysts, which in turn agrees well with the XRD results (Figure 2a). After the reaction, Ni particles appeared in all spent catalysts (Figure 3d–f), with the interplanar crystal spacing of ~2.0 Å for Ni(011) and ~2.2 Å for Ni(111) (Figure 3d'–f'). This indicates that a severe support reduction occurs in the Cu/NiMO_x catalysts. The average Ni particle sizes of the spent Cu/NiAlO_x (24.4 nm, Figure 3d) are much smaller than those of the spent Cu/NiFeO_x (33.3 nm, Figure 3e) and Cu/NiCoO_x (38.9 nm, Figure 3f), which is consistent with the XRD results (Figure 2b) and implies that the Ni agglomeration is more significant over the Cu/NiFeO_x and Cu/NiCoO_x than that of the Cu/NiAlO_x during catalysis.

2.4. XPS Analysis of the Cu/NiMO_x Catalysts

The chemical states of Cu and Ni in the fresh and spent Cu/NiMO_x catalysts were examined by X-ray photoelectron spectroscopy (XPS). The results are displayed in Figure 4. From Cu 2p XPS of the fresh Cu/NiAlO_x, Cu/NiFeO_x and Cu/NiCoO_x catalysts, the characteristic peaks assigned to the Cu²⁺ (Cu 2p_{3/2}) ions appear at 934.8 eV, with satellite peaks at 941–943 eV [37,38]. The other peak, positioned at 933.0 eV, was assigned to the Cu⁺/Cu⁰ species [37,38]. Before reaction, it can be found that the Cu²⁺ and Cu⁺/Cu⁰ species coexisted on the catalysts (Figure 4a). However, after reaction, most of the Cu²⁺ species were reduced to Cu⁺/Cu⁰ species, with the absence of satellite peaks of Cu²⁺ (Figure 4d).

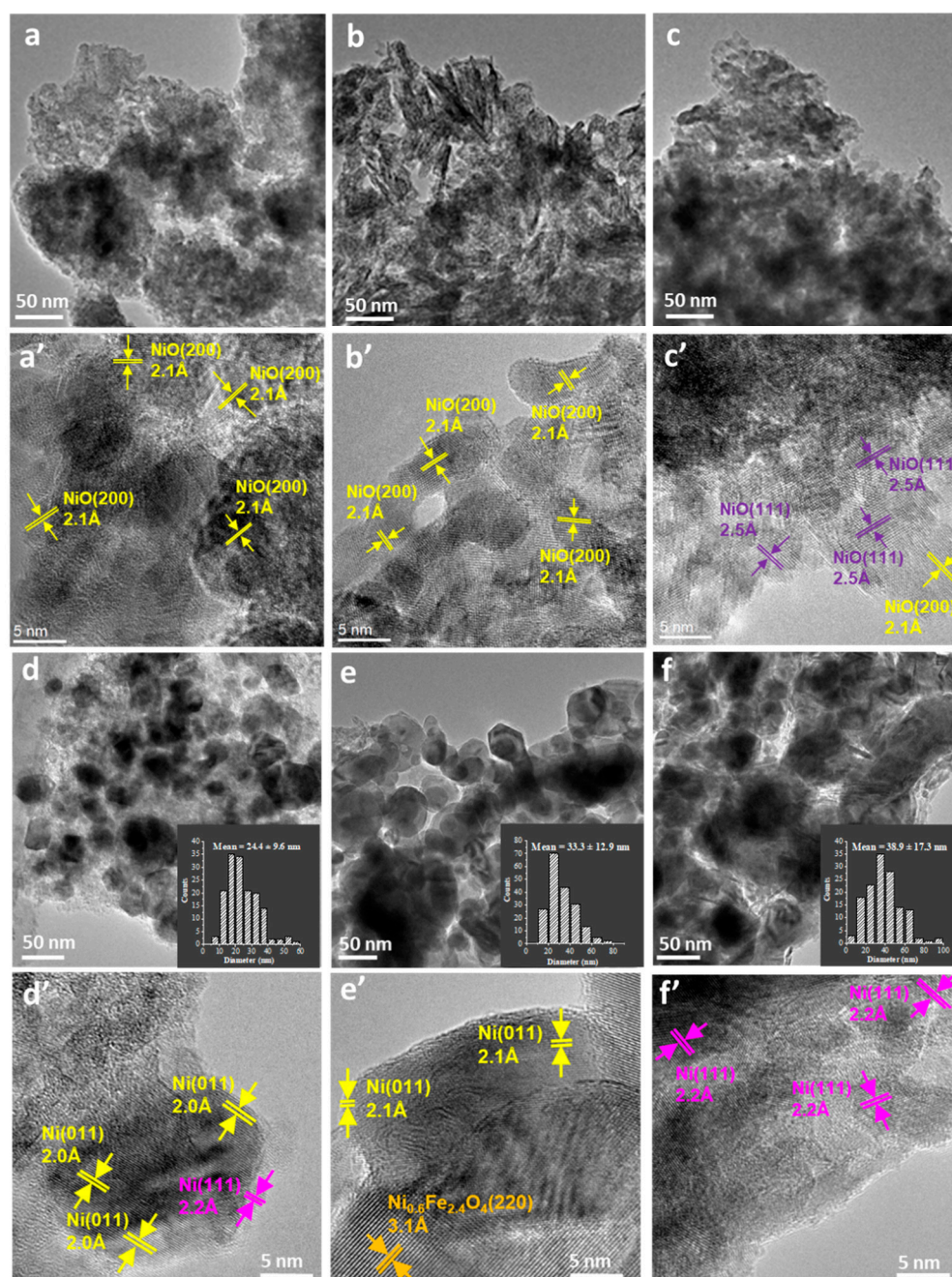


Figure 3. TEM (a–f) and corresponding HRTEM (a’–f’) images of different supported copper catalysts before (a–c) and after (d–f) the reaction. (a,d) Cu/NiAlO_x; (b,e) Cu/NiFeO_x; (c,f) Cu/NiCoO_x.

Since the binding energies of Cu 2p for the Cu⁺ and Cu⁰ are very close to each other, the Auger electron spectroscopy (AES) peaks of Cu LMM were measured to distinguish Cu⁺ from Cu⁰. The peaks positioned at 568.0 eV and 569.7 eV featured the peaks of Cu⁰ and Cu⁺, respectively [39]. Before reaction, Cu⁰ and Cu⁺ species coexisted on all catalysts (Figure 4b). The ratios of Cu⁰/Cu⁺ over the Cu/NiAlO_x, Cu/NiFeO_x and Cu/NiCoO_x are 0.93, 1.34 and 1.81, respectively. After reaction, most of the copper oxides are reduced (Figure 4e), with the ratios of Cu⁰/Cu⁺ increasing up to 4.18, 7.33 and 4.76. The results suggest that Cu species can also be reduced during catalysis. Additionally, Cu⁰ is predominant specie over the surface of the spent catalysts.

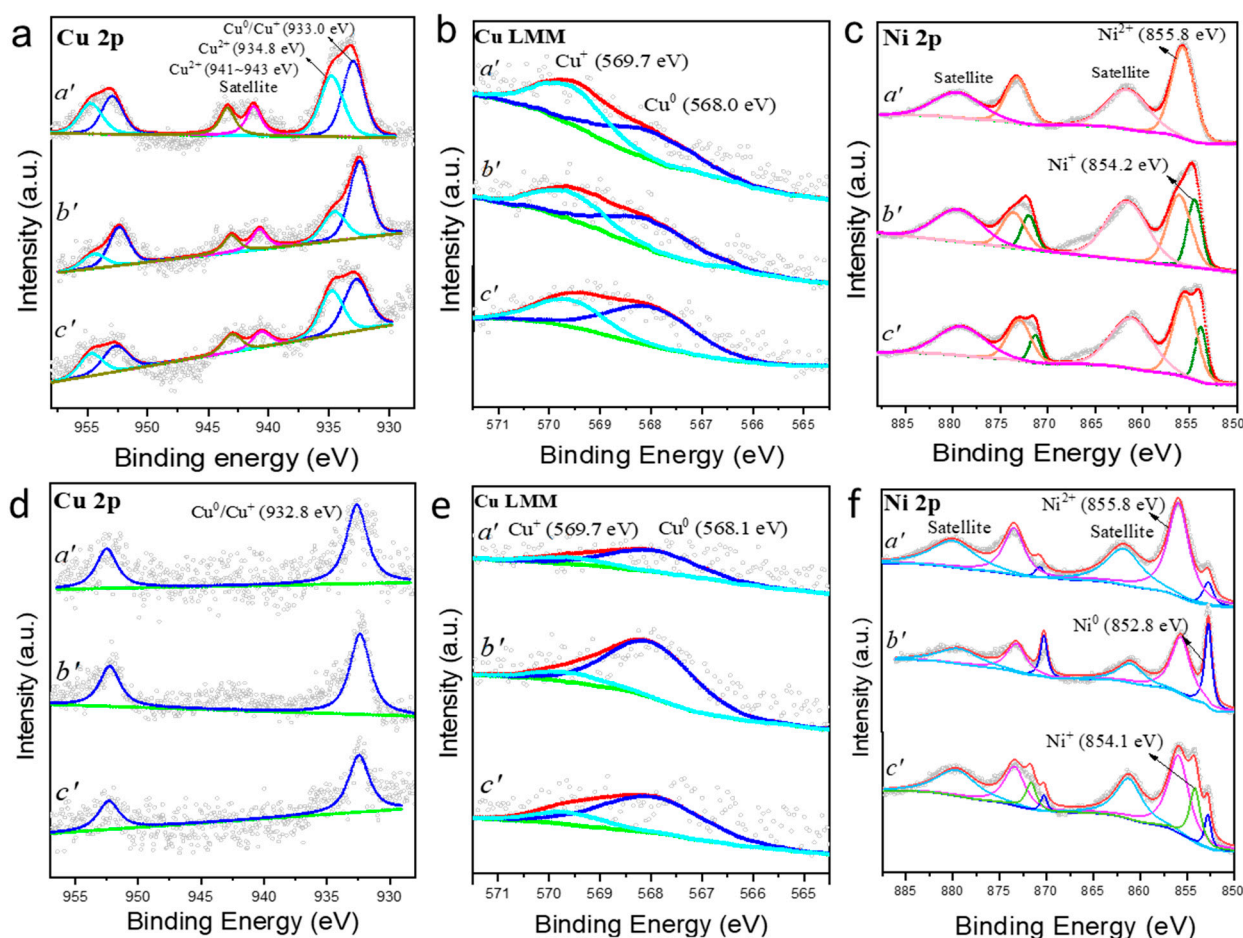


Figure 4. (a,d) Cu 2p XPS, (b,e) Cu LMM and (c,f) Ni 2p XPS of different Cu/NiMO_x catalysts before (a–c) and after (d–f) catalytic tests: (a') Cu/NiAlO_x; (b') Cu/NiFeO_x; (c') Cu/NiCoO_x.

Additionally, in terms of Ni, two strong peaks at 873.3 and 855.8 eV appeared, accompanying two shakeup satellites at 879.7 and 861.8 eV (Figure 4c) and demonstrating the presence of Ni²⁺ [40,41]. Furthermore, the bands at 854.2 eV and 852.8 eV can be assigned to Ni⁺ and Ni⁰, respectively [41,42]. From Figure 4f, the reduction peak of Ni²⁺ to Ni⁰ can be observed in all Cu/NiMO_x catalysts, indicating the severe support reduction of Cu/NiMO_x upon catalysis. This agrees well with the XRD and HRTEM results. However, for the Cu/NiFeO_x and Cu/NiCoO_x, Ni⁺ can be observed in the fresh catalysts (Figure 4c), and the amounts of Ni⁰ species are clearly increased with the spent Cu/NiFeO_x and Cu/NiCoO_x in comparison with those of the Cu/NiAlO_x. This indicates that Cu/NiFeO_x and Cu/NiCoO_x possess much stronger reducibility, which might cause the agglomeration of metal particles and the severe destruction of support, in turn leading to poor stability of the catalysts [43].

2.5. H₂-TPR Results of the Cu/NiMO_x Catalysts

Hydrogen temperature programmed reduction (H₂-TPR) was conducted to measure the reducibility of Cu/NiMO_x catalysts. As shown in Figure 5, two major consumption peaks were observed in all catalysts. The peaks at 150–246 °C can be attributed to the reduction of copper oxides [33,38]. This suggests that the Cu species is easily reduced under the reaction conditions (280 °C, 2 MPa). However, the reduction temperature of copper oxides over the Cu/NiAlO_x shifted from 246 °C to 177 °C (Cu/NiFeO_x) and 186 °C (Cu/NiCoO_x), indicating that Cu is easier to reduce than the latter two catalysts. Furthermore, wide and broad peaks are attributed to support reduction shifts from 450–750 °C for Cu/NiAlO_x to 200–500 °C for Cu/NiFeO_x and Cu/NiCoO_x [44–46], pointing to the facile

reducibility of Cu/NiFeO_x and Cu/NiCoO_x under H₂ atmosphere and agreeing well with the XPS results.

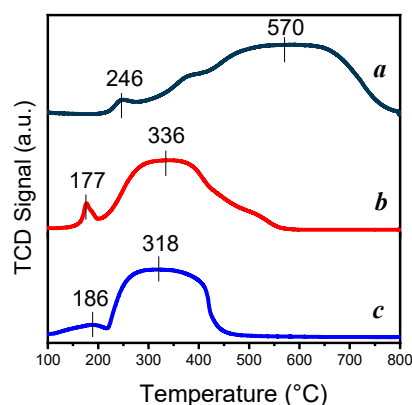


Figure 5. H₂-TPR profiles of different supported copper catalysts: (a) Cu/NiAlO_x; (b) Cu/NiFeO_x; (c) Cu/NiCoO_x.

2.6. CO₂/NH₃-TPD Results

The acid/base sites are reported to play an essential role in modulating the catalytic performance, especially when tailoring the selectivity of the Guerbet coupling process [47,48]. As the Cu content is similarly low (~1.5 wt.%) in all catalysts, the acid/base property is largely derived from the corresponding supports. Thus, to evaluate the acid/base properties, CO₂-TPD and NH₃-TPD measurements were conducted for the different Ni-based oxides. Figure 6a depicts the CO₂-TPD profiles of the above NiMO_x supports. Three types of basic sites (i.e., weak basic site: <300 °C, medium basic site: 300~500 °C and strong basic site: >500 °C) can be observed in the profiles [41,49]. The specific amounts of each basic site were calculated by integrating the corresponding peak areas and are summarized in Table 2. Amongst these, the NiAlO_x possesses the largest amount of basic sites, with weak basic sites of 76.7 μmol/g, medium basic sites of 280.9 μmol/g and strong basic sites of 56.2 μmol/g. Whereas for the NiFeO_x and NiCoO_x, a clear decrease in the amounts of basic sites can be observed, with total basicity of 110~130 μmol/g.

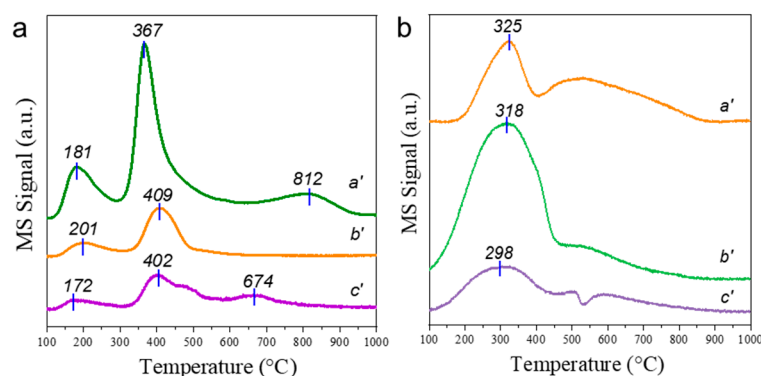


Figure 6. (a) CO₂-TPD and (b) NH₃-TPD profiles of different Ni-based supports: (a') NiAlO_x; (b') NiFeO_x; (c') NiCoO_x.

Table 2. The acid/base properties of different Ni-based supports.

Entry	Samples	Basic Sites (μmol/g) ^a			Acidic Sites (μmol/g) ^b	
		Weak Basic Sites	Medium Basic Sites	Strong Basic Sites	Weak Acidic Sites	Strong Acidic Sites
1	NiAlO _x	76.7	280.9	56.2	42.0	53.2
2	NiFeO _x	22.6	88.0	0	131.6	23.5
3	NiCoO _x	29.6	79.7	20.3	37.3	18.6

^a As determined by CO₂-TPD; ^b As determined by NH₃-TPD.

Beyond the basic sites, the amount and strength of the acid sites are also essential for tailoring the products distributions [27,50]. Figure 6b shows the NH_3 -TPD profiles of the three NiMO_x supports. From these results, all of the samples show roughly two types of acid sites (i.e., weak acid sites: $<450^\circ\text{C}$ and strong acid sites: $>450^\circ\text{C}$) [41]. The number of each acid site over the different NiMO_x are summarized in Table 2. For the NiFeO_x , the largest amount of weak acidic sites (131.6 $\mu\text{mol/g}$) is shown when compared with those of NiAlO_x (42.0 $\mu\text{mol/g}$) and NiCoO_x (37.3 $\mu\text{mol/g}$). This might decrease the selectivity of the Guerbet coupling process, as the acid sites are often reported to be beneficial for the dehydration reaction in producing ether and ethyl acetate [19,34].

2.7. Catalytic Performance of Different Catalysts in Ethanol Coupling to Butanol

The catalytic performances of ethanol coupling to butanol over the Cu/NiMO_x catalysts were accessed in a continuous fixed-bed reactor at 280°C , 2 MPa of N_2 . Among the evaluated catalysts, Cu/NiAlO_x displays the best performance in terms of activity, selectivity and stability, with a sustained ethanol conversion of $\sim 35\%$, butanol productivity (BP) of $\sim 719.3 \text{ mmol}\cdot\text{g}_{\text{cat}}^{-1}\cdot\text{h}^{-1}$, and butanol selectivity of 25% in a time-on-stream (TOS) of 110 h (Figure 7a). Ether, ethyl acetate, ethyl butyl ether, ethyl butyrate, butanal, etc. are detected as the by-products. For the Cu/NiFeO_x , a progressive drop-in activity from an initial ethanol conversion of 34% to 10% and a lower BP of $139.7 \text{ mmol}\cdot\text{g}_{\text{cat}}^{-1}\cdot\text{h}^{-1}$ are observed upon a TOS of 110 h (Figure 7b). Considerable amounts of ethyl acetate and ether, rather than butanol, are obtained as the main products after catalysis, indicating a poor performance of Cu/NiFeO_x in terms of butanol selectivity ($<5\%$). For the Cu/NiCoO_x , a high initial ethanol conversion of 43.4% and a quick decrease in activity from an initial ethanol conversion of 43.4% to 25% (at a TOS of 12 h) and further to 10% (at a TOS of 110 h) are observed during catalysis (Figure 7c). A sustained butanol selectivity in the range of 15% to 21%, is observed for the reaction, with a BP of $535.2 \text{ mmol}\cdot\text{g}_{\text{cat}}^{-1}\cdot\text{h}^{-1}$ over the Cu/NiCoO_x . Although a sustained butanol selectivity of 15~21% can be observed for Cu/NiCoO_x , a gradual deactivation of Cu/NiCoO_x , in particular with respect to its activity, is illustrated by the long-term 110 h continuous run. It is clear, therefore, that the catalytic performances of the Cu/NiMO_x catalysts for the Guerbet coupling reaction were affected by the support effect. Cu/NiAlO_x outperforms in catalytic performance in terms of activity, selectivity and stability, when compared with Cu/NiFeO_x and Cu/NiCoO_x .

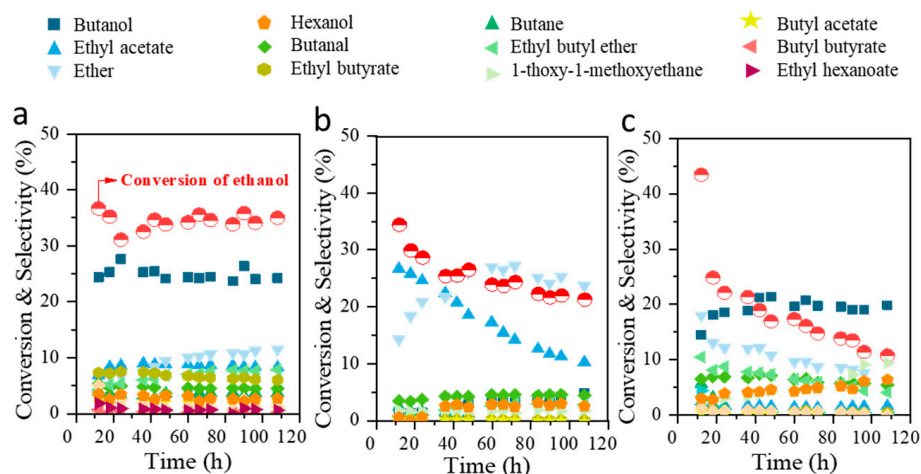
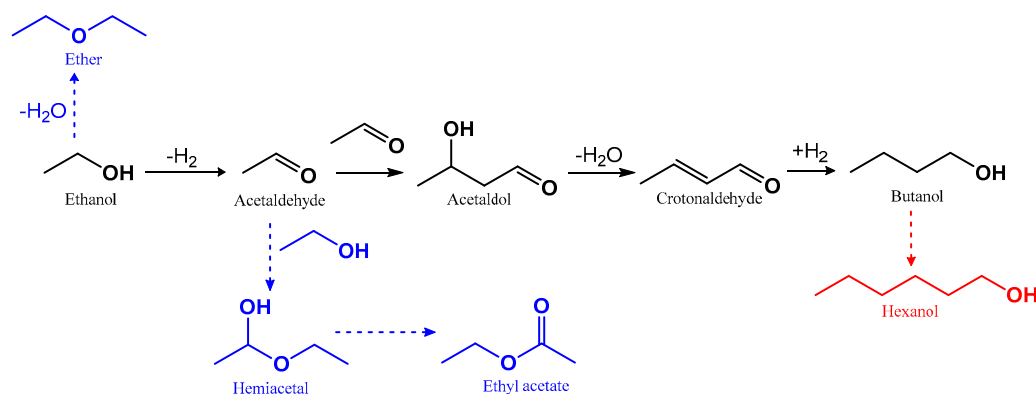


Figure 7. Catalytic performances of different supported Cu catalysts for ethanol coupling to butanol: (a) Cu/NiAlO_x ; (b) Cu/NiFeO_x ; (c) Cu/NiCoO_x . Reaction conditions: catalyst: 1 g, pressure of N_2 : 2 MPa, reaction temperature: 280°C , GHSV: 692 h^{-1} , LHSV: 4.8 h^{-1} .

3. Discussion

According to our previous studies, the support itself displays poor catalytic activity for ethanol upgrading to higher alcohols [33,34]. The introduction of an appropriate amount of Cu species (>0.75 wt.%) can significantly increase the active sites for ethanol dehydrogenation and crotonaldehyde hydrogenation, thereby enhancing the ethanol conversion and the production of the target product [33]. In this work, the addition of ~1.5 wt.% Cu is adequate for ethanol transformation, as the initial ethanol conversion over the three Cu/NiMO_x catalysts did not show many differences (Figure 7). However, after a TOS of 110 h, clear catalyst deactivation appeared over the Cu/NiFeO_x and Cu/NiCoO_x but not the Cu/NiAlO_x, indicating that the support effect greatly affected the stability of the catalysts. Based on our characterization results, all catalysts show different degrees of reduction under the reaction conditions, as proved by XRD (Figure 2), TEM (Figure 3) and XPS (Figure 4). However, over the Cu/NiFeO_x and Cu/NiCoO_x, a stronger and clear reducibility was observed, as proved by XPS (Figure 4) and H₂-TPR (Figure 5). This might cause the severe support deconstruction under H₂ atmosphere and induce the agglomeration of Cu/Ni particles, leading to poor stability of the corresponding catalysts.

Furthermore, in terms of butanol selectivity, the product distribution was strongly dependent on the support selection. Over the Cu/NiAlO_x, a decent butanol selectivity can be obtained (Figure 7a), whereas over the Cu/NiFeO_x, ethyl acetate and ether were produced as the main products (Figure 7b). Based on the previous reports, the product distribution of the Guerbet coupling process was highly correlated with the acid–base properties of the catalysts [51–53]. Additionally, their catalytic performances are boosted by an appropriate acid–base cooperation [40,52]. In our work, the CO₂/NH₃-TPD results indicate that different Ni-based supports show quite different amounts and strengths among the acid/base sites (Figure 6). Among these, the NiAlO_x-supported Cu catalyst possesses the optimal acid and basic sites, with a majority of them either of weak or medium strength. This is proposed to be of benefit when catalyzing aldol condensation and improving the butanol selectivity [51,53]. Cu/NiCoO_x is inferior to Cu/NiAlO_x, showing a lower butanol selectivity of between 15–21% during a TOS of 110 h. It can be deduced that the decreased basic and acid sites lead to a reduction of C–C coupling production, thus decreasing the butanol selectivity. However, for the Cu/NiFeO_x, the presence of excessive acid sites leads to a severe dehydration process, which greatly improves the generation of dehydration product, such as ethyl acetate and ether [54]. The proposed reaction mechanism of the Cu/NiMO_x catalysts for the Guerbet coupling process is presented in Scheme 1, from which we can see that multifunctional sites are required for the synergistic catalysis of the Guerbet coupling process. The Cu species provide active sites for ethanol dehydrogenation and crotonaldehyde hydrogenation, while supports with appropriate acid and/or basic properties supply active sites for the promotion of aldol condensation to produce butanol.



Scheme 1. The reaction path of the Guerbet coupling process over the Cu/NiMO_x catalysts.

To dynamically track the intermediates during the ethanol coupling process, in situ DRIFTS measurements using ethanol as the probe molecule were conducted for different Cu/NiMO_x catalysts (Figure 8). The spectra were obtained by subtracting the background obtained at room temperature and atmospheric pressure. After introducing ethanol with a He flow at 25 °C, the IR cell temperature was gradually elevated from 25 °C to 300 °C at a heating ramp of 10 °C/min. Simultaneously, the spectra were collected at respective steady states of 100, 150, 200, 250, and 300 °C. Notably, two featured bands at around 1055 and 1126 cm⁻¹, corresponding to the C-O stretching vibrations of adsorbed ethoxide [29,51]; a band at around 1253 cm⁻¹ that can be attributed to the δ(C-OH) of adsorbed ethanol/3-hydroxybutanal/butanol [26]; and two bands at around 1632 and 1758 cm⁻¹ attributed to C=C and C=O groups of adsorbed crotonaldehyde [29,55]. For the Cu/NiAlO_x (Figure 8a), as the temperature increased from 25 to 300 °C, the bands at around 1126 cm⁻¹ and 1079 cm⁻¹ greatly decayed, while the band at 1650 cm⁻¹ and 1758 cm⁻¹ appeared and developed, indicating the consumption of adsorbed ethoxide and the production of intermediates such as 3-hydroxybutanal and crotonaldehyde. Nevertheless, minor changes in C-O, C=C and C=O vibrations are observed for Cu/NiFeO_x (Figure 8b) and Cu/NiCoO_x (Figure 8c) even as the temperature increased up to 250 °C. This implies a lower reactivity and butanol selectivity for Cu/NiFeO_x and Cu/NiCoO_x than of Cu/NiAlO_x, which agrees well with the catalytic performances.

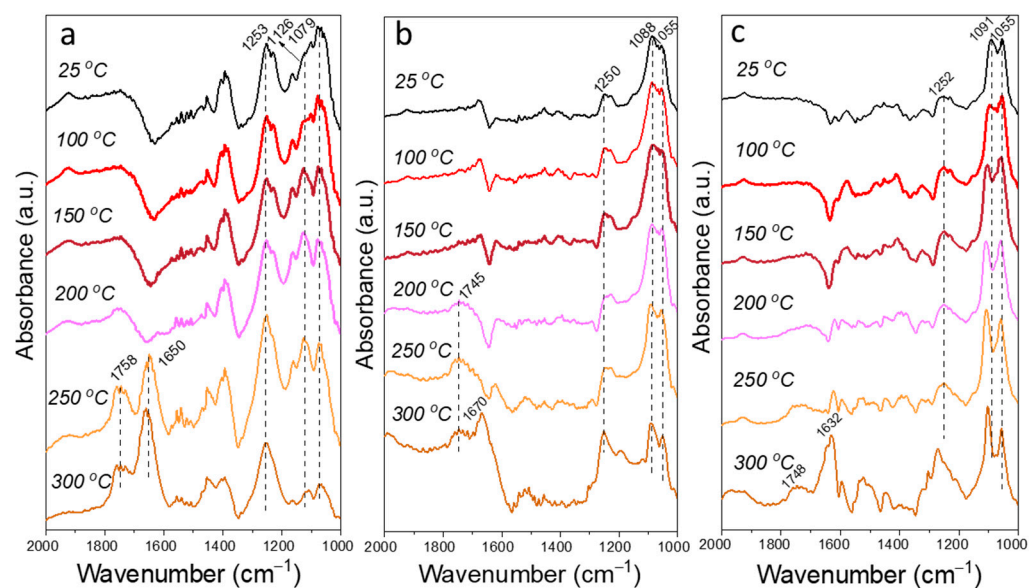


Figure 8. In situ DRIFTS of ethanol over different supported Cu catalysts in the range of 1000–2000 cm⁻¹: (a) Cu/NiAlO_x; (b) Cu/NiFeO_x; (c) Cu/NiCoO_x.

4. Materials and Methods

4.1. Materials

Copper nitrate trihydrate, Nickel nitrate hexahydrate, Ferric nitrate nonahydrate, Cobalt nitrate hexahydrate, butanol, ethanol and methanol were purchased from Sinopharm company (Beijing, China). Sodium hydroxide, sodium carbonate, aluminum nitrate hydrate, ethyl acetate and ortho-xylene were purchased from Aladdin Industrial Corporation (Shanghai, China). All chemicals were utilized without purification process.

4.2. Preparation of the Catalysts

4.2.1. Synthesis of Different Ni-Based HTs

Different Ni-based HTs were prepared via the co-precipitation method. Amounts of 0.105 mol of Ni(NO₃)₂·6H₂O and 0.035 mol of M(NO₃)₃·xH₂O (M = Al, Fe, Co) were mixed with 150 mL of ultrapure water to obtain solution A. Amounts of 0.057 mol of Na₂CO₃ and 0.219 mol of NaOH were mixed with 150 mL of ultrapure water to obtain solution

B. In a water bath at 80 °C, solution A was dropwise added into solution B with a rate of 50 mL/min using a constant flow pump. Then, the gel was stirred and aged at 80 °C for 24 h. The resulting suspension was filtered and exhaustively washed with deionized water until the pH of the filtrate reached 7. Then the filter cake was dried in an oven at 80 °C for 8 h to obtain NiM-HT (M = Al, Fe, Co).

4.2.2. Synthesis of Ni-Based HT-Derived Cu Catalysts

The different supported Cu catalysts were synthesized through deposition precipitation method. Firstly, 2 g of the NiM-HT powders and 100 mL of deionized water were added into a round-bottom flask. Then, the pH was adjusted to ~10 by solution of Na₂CO₃. Subsequently, 80 mg of Cu(NO₃)₂·3H₂O was added into the flask and the solution was heated to 80 °C. The reaction was processed for 2 h under constant stirring. Then, the product was filtered and washed with large amounts of water. Before tests, the samples were dried at 80 °C for 8 h and calcined at 300 °C for 2 h. The obtained samples were denoted as Cu/NiMO_x (M = Al, Fe, Co).

4.3. Catalytic Evaluation

The catalytic transformation of ethanol to butanol was carried out in a fixed-bed reactor with an inner diameter of 10 mm and a length of 660 mm. The reaction process was performed at specified conditions with N₂ as the carrier gas. For each test, 1 g of the catalyst was loaded into the middle of the reactor. Both ends were filled with quartz sand. Before the test, N₂ was introduced into the system and the pressure was maintained with a back-pressure regulator. Then, the temperature was programmed to increase to a specific value, with a heating ramp of 5 °C/min. Ethanol was then introduced into the system with constant liquid hourly space velocity (LHSV) by using a plunger pump (NP-KX-210). The analysis of products was conducted at an interval of 12 h. An Agilent 7890B chromatograph and mass spectrometer (Agilent 5977B MSD) were used offline to detect the reactants and products and were equipped with a flame ionization detector (FID) and an HP-5 capillary column (30 m × 0.32 mm). O-xylene was used as the internal standard.

4.4. Characterization

The actual Cu loadings were measured with an inductively coupled plasma atomic emission spectroscopy (ICP-AES) on an IRIS Intrepid II XSP instrument (Thermo Electron Corporation, Waltham, MA, USA). A Quantachrome NT3LX-2 instrument (FL, USA) was utilized to determine the textural properties of the catalysts by N₂ physical adsorption-desorption at −196 °C. The phase structure and crystallinity of the fresh/spent catalysts were analyzed using X-ray diffraction (XRD). The spectra were recorded on a PW3040/60 X'Pert PRO (PANalytical, Almelo, The Netherlands) diffractometer with a Cu Kα X-ray source radiation at 40 kV and 30 mA in the range of 10°~90°. Transmission electron microscopy (TEM) and high-resolution transmission electron microscopy (HRTEM) were recorded on a JEOL JEM-2100F microscope (Tokyo, Japan) and Oxford detectors at 200 kV, respectively. The X-ray photoelectron spectroscopy (XPS) and X-ray-induced Auger electron spectroscopy (XAES) were conducted on an ESCALAB 250Xi X-ray photoelectron spectrometer (Thermo Fisher Scientific, Madison, WI, USA) connected to a monochromatic Al and double anode Al/Mg ray source. The C 1s at 284.6 eV was recorded to adjust the binding energies of the other investigated elements. Hydrogen temperature-programmed reduction (H₂-TPR) experiments were studied on a Micromeritics Autochem II 2920 chemisorber (Norcross, GA, USA). For each test, the catalyst (~100 mg) was treated at 300 °C for 1 h in a quartz U-tube reactor with a He gas stream (30 mL/min). After cooling to room temperature, a 10% H₂/Ar flow (30 mL/min) was introduced into the system, and the sample was heated to 800 °C at a ramping rate of 10 °C/min. The H₂-TPR signal was recorded by TCD and MS detector simultaneously. The basicity and acidity of catalysts were measured by temperature-programmed desorption (TPD) of CO₂/NH₃ on a Micromeritics Autochem II 2920 (Norcross, GA, USA) equipped with a thermal conductivity detector (TCD) and MS

detector. Prior to the measurements, ~100 mg of catalyst was treated at 300 °C for 1 h in He (50 mL/min). Then, the temperature was cooled to 100 °C and the sample was adsorbed and saturated with 10% CO₂/He or NH₃/He flow pulse (30 mL/min) for 20 times. Subsequently, the sample was purged with He (30 mL/min) for 30 min, and a CO₂/NH₃-TPD signal was recorded from 100 to 1000 °C, with a heating rate of 10 °C/min with a TCD and an MS detector. In situ diffuse reflectance infrared Fourier-transformed spectroscopy (DRIFTS) was performed on a Bruker INVENIO Fourier-transform infrared spectrometer (Bruker, Karlsruhe, Germany), equipped with an MCT detector. Before the experiment, the catalyst was treated at 300 °C for 0.5 h. After cooling to room temperature, the background spectrum was recorded, and ethanol was introduced into the cell with the assistance of a He flow (30 mL/min). Then, the reaction temperature was increased gradually with a heating rate of 10 °C/min. After achieving a fixed temperature, the spectra were collected at respective steady states of 100, 150, 200, 250, and 300 °C.

5. Conclusions

In summary, we have prepared a series of supported Cu catalysts derived from Ni-based hydrotalcite (Cu/NiAlO_x, Cu/NiFeO_x and Cu/NiCoO_x) via the hydrothermal precipitation method. The catalytic performances for ethanol coupling to butanol were evaluated and compared with three different catalysts at the continuous fixed-bed reactor. The support effect was found to greatly influence the catalytic performance in terms of selectivity and stability. Notably, Cu/NiAlO_x outperforms in the butanol yield and long-term stability, when compared with Cu/NiFeO_x and Cu/NiCoO_x. Furthermore, we have demonstrated that the appropriate acid–base combinations in close proximity within the support are pivotal for achieving a decent butanol selectivity in the Guerbet coupling process, while the deconstruction of the support by reduction during catalysis is the main reason for the deactivation of catalysts. Our findings may be of great help for the rational design of efficient heterogeneous catalysts with combination of multiple functional sites that can afford improved performance, especially in terms of selectivity and stability, in the tandem conversion of biomass-derived small substrates, including ethanol and beyond.

Author Contributions: Conceptualization and supervision, Y.T.; data curation and investigation, Y.X. and J.L.; methodology, X.C.; software, F.B.; writing—review and editing, W.L.; resources and review, Y.D. All authors have read and agreed to the published version of the manuscript.

Funding: This research was funded by the National Natural Science Foundation of China (22102149).

Institutional Review Board Statement: Not applicable.

Informed Consent Statement: Not applicable.

Data Availability Statement: Data are available upon request from the corresponding authors.

Acknowledgments: The authors are grateful for the support of the public testing platform of Zhejiang Normal University and the Dalian Institute of Chemical Physics, Chinese Academy of Sciences.

Conflicts of Interest: The authors declare no conflict of interest.

References

1. Queneau, Y.; Han, B. Biomass: Renewable carbon resource for chemical and energy industry. *Innovation* **2022**, *3*, 100184. [[CrossRef](#)]
2. Antar, M.; Lyu, D.; Nazari, M.; Shah, A.; Zhou, X.; Smith, D.L. Biomass for a sustainable bioeconomy: An overview of world biomass production and utilization. *Renew. Sust. Energ. Rev.* **2021**, *139*, 110691. [[CrossRef](#)]
3. Rass-Hansen, J.; Falsig, H.; Jørgensen, B.; Christensen, C.H. Bioethanol: Fuel or feedstock. *J. Chem. Technol. Biot.* **2007**, *82*, 329–333. [[CrossRef](#)]
4. Angelici, C.; Weckhuysen, B.M.; Bruijninx, P.C. Chemocatalytic conversion of ethanol into butadiene and other bulk chemicals. *ChemSusChem* **2013**, *6*, 1595–1614. [[CrossRef](#)] [[PubMed](#)]
5. Phillips, S.D.; Jones, S.B.; Meyer, P.A.; Snowden-Swan, L.J. Techno-economic analysis of cellulosic ethanol conversion to fuel and chemicals. *Biofuel. Bioprod. Biorefin.* **2022**, *16*, 640–652. [[CrossRef](#)]
6. Sun, J.; Wang, Y. Recent advances in catalytic conversion of ethanol to chemicals. *ACS Catal.* **2014**, *4*, 1078–1090. [[CrossRef](#)]

7. Chung, S.H.; Li, T.; Shoinkhorova, T.; Komaty, S.; Ramirez, A.; Mukhambetov, I.; Abou-Hamad, E.; Shterk, G.; Telalovic, S.; Dikhtiarenko, A.; et al. Origin of active sites on silica–magnesia catalysts and control of reactive environment in the one-step ethanol-to-butadiene process. *Nat. Catal.* **2023**, *6*, 363–376. [[CrossRef](#)]
8. Mück, J.; Kocík, J.; Hájek, M.; Tišler, Z.; Frolich, K.; Kašpárek, A. Transition metals promoting Mg–Al mixed oxides for conversion of ethanol to butanol and other valuable products: Reaction pathways. *Appl. Catal. A-Gen.* **2021**, *626*, 118380. [[CrossRef](#)]
9. Dowson, G.R.; Haddow, M.F.; Lee, J.; Wingad, R.L.; Wass, D.F. Catalytic conversion of ethanol into an advanced biofuel: Unprecedented selectivity for n-butanol. *Angew. Chem. Int. Ed.* **2013**, *52*, 9005–9008. [[CrossRef](#)]
10. Jiang, D.; Fang, G.; Tong, Y.; Wu, X.; Wang, Y.; Hong, D.; Leng, W.; Liang, Z.; Tu, P.; Liu, L.; et al. Multifunctional Pd@UiO-66 catalysts for continuous catalytic upgrading of ethanol to n-butanol. *ACS Catal.* **2018**, *8*, 11973–11978. [[CrossRef](#)]
11. Zhang, Q.; Dong, J.; Liu, Y.; Wang, Y.; Cao, Y. Towards a green bulk-scale biobutanol from bioethanol upgrading. *J. Energy Chem.* **2016**, *25*, 907–910. [[CrossRef](#)]
12. Tsuchida, T.; Sakuma, S.; Takeguchi, T.; Ueda, W. Direct synthesis of n-butanol from ethanol over nonstoichiometric hydroxyapatite. *Ind. Eng. Chem. Res.* **2006**, *45*, 8634–8642. [[CrossRef](#)]
13. Veza, I.; Said, M.F.M.; Latiff, Z.A. Recent advances in butanol production by acetone-butanol-ethanol (ABE) fermentation. *Biomass Bioenergy* **2021**, *144*, 105919. [[CrossRef](#)]
14. Yuan, B.; Zhang, J.; An, Z.; Zhu, Y.; Shu, X.; Song, H.; Xiang, X.; Wang, W.; Jing, Y.; Zheng, L.; et al. Atomic Ru catalysis for ethanol coupling to C4+ alcohols. *Appl. Catal. B* **2022**, *309*, 121271. [[CrossRef](#)]
15. Lopez-Olmos, C.; Morales, M.V.; Guerrero-Ruiz, A.; Ramirez-Barria, C.; Asedegbega-Nieto, E.; Rodriguez-Ramos, I. Continuous gas-phase condensation of bioethanol to 1-butanol over bifunctional Pd/Mg and Pd/Mg-carbon catalysts. *ChemSusChem* **2018**, *11*, 3502–3511. [[CrossRef](#)] [[PubMed](#)]
16. Pang, J.; Zheng, M.; He, L.; Li, L.; Pan, X.; Wang, A.; Wang, X.; Zhang, T. Upgrading ethanol to n-butanol over highly dispersed Ni–MgAlO catalysts. *J. Catal.* **2016**, *344*, 184–193. [[CrossRef](#)]
17. Fu, S.; Shao, Z.; Wang, Y.; Liu, Q. Manganese-catalyzed upgrading of ethanol into 1-butanol. *J. Am. Chem. Soc.* **2017**, *139*, 11941–11948. [[CrossRef](#)]
18. Perrone, O.M.; Lobefaro, F.; Aresta, M.; Nocito, F.; Boscolo, M.; Dibenedetto, A. Butanol synthesis from ethanol over CuMgAl mixed oxides modified with palladium (II) and indium (III). *Fuel Process. Technol.* **2018**, *177*, 353–357. [[CrossRef](#)]
19. Hanspal, S.; Young, Z.D.; Prillaman, J.T.; Davis, R.J. Influence of surface acid and base sites on the Guerbet coupling of ethanol to butanol over metal phosphate catalysts. *J. Catal.* **2017**, *352*, 182–190. [[CrossRef](#)]
20. Osman, M.B.; Krafft, J.; Thomas, C.; Yoshioka, T.; Kubo, J.; Costentin, G. Importance of the nature of the active acid/base pairs of hydroxyapatite involved in the catalytic transformation of ethanol to n-butanol revealed by operando drifts. *ChemCatChem* **2019**, *11*, 1765–1778. [[CrossRef](#)]
21. Metzker, G.; Vargas, J.; de Lima, L.; Perrone, O.; Siqueira, M.; Varanda, L.; Boscolo, M. First row transition metals on the ethanol Guerbet reaction: Products distribution and structural behavior of mixed metal oxides as catalysts. *Appl. Catal. A-Gen.* **2021**, *623*, 118272. [[CrossRef](#)]
22. Cheng, F.; Guo, H.; Cui, J.; Hou, B.; Li, D. Guerbet reaction of methanol and ethanol catalyzed by CuMgAlO mixed oxides: Effect of M^{2+}/Al^{3+} ratio. *J. Fuel Chem. Technol.* **2018**, *46*, 1472–1481. [[CrossRef](#)]
23. Yang, C.; Meng, Z. Bimolecular condensation of ethanol to 1-butanol catalyzed by alkali cation zeolites. *J. Catal.* **1993**, *142*, 37–44. [[CrossRef](#)]
24. Xu, B.; Yang, C.; Meng, Z. Modification of NaX zeolite and its relation to reactivity for ethanol condensation. *Chin. J. Catal.* **1994**, *15*, 482–486.
25. Seekhiaw, P.; Pinthong, P.; Praserttham, P.; Jongsomjit, B. Optimal conditions for butanol production from ethanol over MgAlO catalyst derived from Mg–Al layer double hydroxides. *J. Oleo. Sci.* **2022**, *71*, 141–149. [[CrossRef](#)] [[PubMed](#)]
26. Zhang, J.; Shi, K.; Zhu, Y.; An, Z.; Wang, W.; Ma, X.; Shu, X.; Song, H.; Xiang, X.; He, J. Interfacial sites in Ag supported layered double oxide for dehydrogenation coupling of ethanol to n-butanol. *ChemistryOpen* **2021**, *10*, 1095–1103. [[CrossRef](#)]
27. Cuello-Penalosa, P.A.; Dastidar, R.G.; Wang, S.; Du, Y.; Lanci, M.P.; Wooler, B.; Kliewer, C.E.; Hermans, I.; Dumesic, J.A.; Huber, G.W. Ethanol to distillate-range molecules using Cu/Mg_xAlO_y catalysts with low Cu loadings. *Appl. Catal. B* **2022**, *304*, 120984. [[CrossRef](#)]
28. Marcu, I.; Tanchoux, N.; Fajula, F.; Tichit, D. Catalytic conversion of ethanol into butanol over M–Mg–Al mixed oxide catalysts (M = Pd, Ag, Mn, Fe, Cu, Sm, Yb) obtained from LDH precursors. *Catal. Lett.* **2012**, *143*, 23–30. [[CrossRef](#)]
29. Wang, Z.; Yin, M.; Pang, J.; Li, X.; Xing, Y.; Su, Y.; Liu, S.; Liu, X.; Wu, P.; Zheng, M.; et al. Active and stable Cu doped NiMgAlO catalysts for upgrading ethanol to n-butanol. *J. Energy Chem.* **2022**, *72*, 306–317. [[CrossRef](#)]
30. Benito, P.; Vaccari, A.; Antonetti, C.; Licursi, D.; Schiaroli, N.; Rodriguez-Castellón, E.; Galletti, A.M.R. Tunable copper-hydroxalcalite derived mixed oxides for sustainable ethanol condensation to n-butanol in liquid phase. *J. Clean. Prod.* **2019**, *209*, 1614–1623. [[CrossRef](#)]
31. León, M.; Díaz, E.; Ordóñez, S. Ethanol catalytic condensation over Mg–Al mixed oxides derived from Hydroxalcalites. *Catal. Today* **2011**, *164*, 436–442. [[CrossRef](#)]
32. Di Cosimo, J.I.; Díez, V.K.; Xu, M.; Iglesia, E.; Apesteguía, C.R. Structure and surface and catalytic properties of Mg–Al basic oxides. *J. Catal.* **1998**, *178*, 499–510. [[CrossRef](#)]

33. Li, J.; Lin, L.; Tan, Y.; Wang, S.; Yang, W.; Chen, X.; Luo, W.; Ding, Y. High performing and stable Cu/NiAlO_x catalysts for the continuous catalytic conversion of ethanol into butanol. *ChemCatChem* **2022**, *14*, e202200539. [[CrossRef](#)]
34. Liu, Z.; Li, J.; Tan, Y.; Guo, L.; Ding, Y. Copper supported on MgAlO_x and ZnAlO_x porous mixed-oxides for conversion of bioethanol via Guerbet coupling reaction. *Catalysts* **2022**, *12*, 1170. [[CrossRef](#)]
35. Sing, K.S.W.; Williams, R.T. Physisorption hysteresis loops and the characterization of nanoporous materials. *Adsorp. Sci. Technol.* **2004**, *22*, 773–782. [[CrossRef](#)]
36. Balestra, G.; de Maron, J.; Tabanelli, T.; Cavani, F.; Nieto, J.M.L. The selective ethanol Guerbet condensation over alkali metal-doped sepiolite. *Catal. Today* **2023**, *423*, 114013. [[CrossRef](#)]
37. Pang, J.; Zheng, M.; Wang, C.; Yang, X.; Liu, H.; Liu, X.; Sun, J.; Wang, Y.; Zhang, T. Hierarchical echinus-like Cu-MFI catalysts for ethanol dehydrogenation. *ACS Catal.* **2020**, *10*, 13624–13629. [[CrossRef](#)]
38. Lopez-Olmos, C.; Guerrero-Ruiz, A.; Rodríguez-Ramos, I. Optimization of Cu-Ni-Mn-catalysts for the conversion of ethanol to butanol. *Catal. Today* **2020**, *357*, 132–142. [[CrossRef](#)]
39. Sun, C.; Tang, Y.; Gao, F.; Sun, J.; Ma, K.; Tang, C.; Dong, L. Effects of different manganese precursors as promoters on catalytic performance of CuO-MnO_x/TiO₂ catalysts for NO removal by CO. *Phys. Chem. Chem. Phys.* **2015**, *17*, 15996. [[CrossRef](#)]
40. He, J.; Li, X.; Kou, J.; Tao, T.; Shen, X.; Jiang, D.; Lina, L.; Li, X. Catalytic upgrading of ethanol to higher alcohols over nickel-modified Cu-La₂O₃/Al₂O₃ catalysts. *Catal. Sci. Technol.* **2023**, *13*, 170–177. [[CrossRef](#)]
41. Wang, Z.; Pang, J.; Song, L.; Li, X.; Yuan, Q.; Li, X.; Liu, S.; Zheng, M. Conversion of ethanol to n-butanol over NiCeO₂ based catalysts: Effects of metal dispersion and NiCe interactions. *Ind. Eng. Chem. Res.* **2020**, *59*, 22057–22067. [[CrossRef](#)]
42. He, J.; Lin, L.; Liu, M.; Miao, C.; Wu, Z.; Chen, R.; Chen, S.; Chen, T.; Su, Y.; Zhang, T.; et al. A durable Ni/La-Y catalyst for efficient hydrogenation of γ -valerolactone into pentanoic biofuels. *J. Energy Chem.* **2022**, *70*, 347–355. [[CrossRef](#)]
43. Xiao, Y.; Zhan, N.; Li, J.; Tan, Y.; Ding, Y. Highly selective and stable Cu catalysts based on Ni-Al catalytic systems for bioethanol upgrading to n-butanol. *Molecules* **2023**, *28*, 5683. [[CrossRef](#)] [[PubMed](#)]
44. Hernández, W.Y.; De Vlieger, K.; Van Der Voort, P.; Verberckmoes, A. Ni-Cu hydrotalcite-derived mixed oxides as highly selective and stable catalysts for the synthesis of β -branched bioalcohols by the Guerbet reaction. *ChemSusChem* **2016**, *9*, 3196–3205. [[CrossRef](#)]
45. Gao, Y.; Zhao, Z.; Jia, H.; Yang, X.; Lei, X.; Kong, X.; Zhang, F. Partially reduced Ni²⁺, Fe³⁺-layered double hydroxide for ethanol electrocatalysis. *J. Mater. Sci.* **2019**, *54*, 14515–14523. [[CrossRef](#)]
46. Hong, N.N.; Manh, H.K.; Minh, T.L.; Mai, P.P.T.; Hai, N.C.T. Study on spinel-typed catalyst NiCo₂O₄ for total oxidation of toluene. *Vietnam J. Catal. Adsorp.* **2021**, *10*, 101–106. [[CrossRef](#)]
47. Zhu, Q.; Yin, L.; Ji, K.; Li, C.; Wang, B.; Tan, T. Effect of catalyst structure and acid base property on the multiproduct upgrade of ethanol and acetaldehyde to C₄ (butadiene and butanol) over the Y-SiO₂ catalysts. *ACS Sustain. Chem. Eng.* **2020**, *8*, 1555–1565. [[CrossRef](#)]
48. Zhang, J.; Shi, K.; An, Z.; Zhu, Y.; Shu, X.; Song, H.; Xiang, X.; He, J. Acid-base promoted dehydrogenation coupling of ethanol on supported Ag particles. *Ind. Eng. Chem. Res.* **2020**, *59*, 3342–3350. [[CrossRef](#)]
49. Li, J.; Wang, S.; Li, H.; Tan, Y.; Ding, Y. Zn promoted Mg-Al mixed oxides-supported gold nanoclusters for direct oxidative esterification of aldehyde to ester. *Int. J. Mol. Sci.* **2021**, *22*, 8668. [[CrossRef](#)] [[PubMed](#)]
50. Ndou, A.S.; Plint, N.; Coville, N.J. Dimerisation of ethanol to butanol over solid-base catalysts. *Appl. Catal. A-Gen.* **2003**, *251*, 337–345. [[CrossRef](#)]
51. Jiang, D.; Wu, X.; Mao, J.; Ni, J.; Li, X. Continuous catalytic upgrading of ethanol to n-butanol over Cu-CeO₂/AC catalysts. *Chem. Commun.* **2016**, *52*, 13749–13752. [[CrossRef](#)]
52. Wu, X.; Fang, G.; Tong, Y.; Jiang, D.; Liang, Z.; Leng, W.; Liu, L.; Tu, P.; Wang, H.; Ni, J.; et al. Catalytic upgrading of ethanol to n-butanol: A progress in catalyst development. *ChemSusChem* **2018**, *11*, 71–85. [[CrossRef](#)]
53. Petrolini, D.D.; Eagan, N.; Ball, M.R.; Burt, S.P.; Hermans, I.; Huber, G.W.; Dumesic, J.A.; Martins, L. Ethanol condensation at elevated pressure over copper on AlMgO and AlCaO porous mixed-oxide supports. *Catal. Sci. Technol.* **2019**, *9*, 2032–2042. [[CrossRef](#)]
54. Wang, L.; Zhu, W.; Zheng, D.; Yu, X.; Cui, J.; Jia, M.; Zhang, W.; Wang, Z. Direct transformation of ethanol to ethyl acetate on Cu/ZrO₂ catalyst. *Reac. Kinet. Mech. Cat.* **2010**, *101*, 365–375. [[CrossRef](#)]
55. Pacheco, H.; de Souza, E.; Landi, S.; David, M.; Prillaman, J.; Davis, R.; Toniolo, F. Ru promoted MgO and Al-modified MgO for ethanol upgrading. *Top. Catal.* **2019**, *62*, 894–907. [[CrossRef](#)]

Disclaimer/Publisher's Note: The statements, opinions and data contained in all publications are solely those of the individual author(s) and contributor(s) and not of MDPI and/or the editor(s). MDPI and/or the editor(s) disclaim responsibility for any injury to people or property resulting from any ideas, methods, instructions or products referred to in the content.